Front evaporation effects on wicking in two- and three-dimensional porous domains

Eric M. Benner and Dimiter N. Petsev

Phys. Rev. E **98**, 053104 — Published 16 November 2018

DOI: 10.1103/PhysRevE.98.053104

Front Evaporation Effects on Wicking in Two- and Three-Dimensional Porous Domains

Eric M. Benner* and Dimiter N. Petsev†
Department of Chemical and Biological Engineering, and Center for Micro-Engineered Materials, University of New Mexico, Albuquerque, NM 87131, USA
(Dated: October 23, 2018)

We present the equations for wicking in two- and three-dimensional porous media when liquid is evaporating through the wet front using the Green–Ampt saturated capillary flow model in polar and spherical geometries. The time-dependent behavior of two-dimensional wicking influenced by front interface evaporation manifests distinctly from the influence on wicking by normal surface evaporation. This is shown in several ways; notably, the first order effects of the front evaporation, as considered via an evaporation-capillary number, is of a lower order in the front position than normal evaporation. Furthermore, the front evaporation-induced steady states of the front position and bulk velocity vary significantly with the dimensionality of the flow expansion in the porous domain; with respect to the dimensionality, the front position decreases while the bulk velocity increases.

I. INTRODUCTION

Evaporation, gravity, and the geometry of a porous medium, among numerous physical phenomena, have significant effects on capillary flow behavior [1]. These include reducing or enhancing the rate of flow, modifying the saturation profile, and changing the flow symmetry [2–4]. At present, the effects of gravity and geometry on the capillary flow behavior are better understood than evaporation [5, 6]. For thin porous materials, there are three modes of evaporation losses; each are related to the interface through which the evaporation occurs and are accounted for distinctly in the physical model. The dominant mode is commonly through the static surface which is normal to the thin two-dimensional (2D) plane of the porous medium; we refer to this as normal surface evaporation and dealt with this extensively in Ref. [7]. The second mode, which is physically identical to normal surface evaporation but mathematically distinct, occurs through the external boundaries of the porous medium which are within the 2D plane and commonly orthogonal to the flow; this is side boundary evaporation [8]. Finally, evaporation may also occur at the front of the flow through the advancing capillary interface between the wetting and the dry portions of the domain; this is front interface evaporation, and we investigate its' effects on capillary flow in this paper.

Novel technologies are being developed which make use of capillary flows to drive a liquid reacting solvent mixture in small microfluidic and fuel cell devices [9–13]. These flows are sensitive to the effects of evaporation over long timescales, so these microfluidic experiments require accurate predictive fluid models for the rate of liquid advancement and bulk flow into the porous medium under evaporation [7]. The evaporation can also be used as a means of controlling the flow rate through the device [10]. Liquid losses through evaporation from capillary flows should be understood for design of porous containers, wells, and construction materials, in addition to drying porous materials [14–16]. Furthermore, analysis of evaporative cooling processes requires accurate estimates of liquid uptake and saturated volume to couple with heat and mass transfer models for heat loss calculations. In this paper, we present novel analytical solutions for capillary flow through two- and three-dimensional (3D) geometries when effected by front evaporation, specifically.

The effect of the 2D polar and 3D hemispherical geometries on pure saturated wicking are given by Hyväluoma *et al.* [17] and Xiao *et al.* [18], respectively. These solutions, and the one-dimensional (1D) Lucas–Washburn (LW) equation [19, 20], are compared in Ref. [1] showing clear variations in the flow behavior with the dimension of the expansion. Phillip [4] also considers 2D and 3D expanding geometries but for capillary flow with a continuous saturation profile. In all the studies, it has been observed that a greater dimensionality of the expansion reduces the rate of advancement of the wet front, but increases the volumetric flow into the porous medium. These effects are further accelerated by evaporation [7]. We are interested in quantifying these variations under front evaporation beyond that of the more prevalent normal surface evaporation.

Occurring through physically different interfaces of the wetted porous domain, the three modes of evaporation—normal, and side, and front—are introduced in Ref. [8], where it is shown that the normal and front evaporation behave differently as a function of time and dimensionless evaporation-capillary number—the ratio of the evaporation rate to the intrinsic capillary flow rate. All three evaporation types are relevant to thin porous domains, which may have flows that are either 1D (constant cross-section) or 2D (expanding flow) in character. For fully 3D porous domains, the infinitely thin approximation is invalid and normal surface evaporation is not a physically relevant model, but side and front evaporation may

*Electronic address: ebenner@unm.edu
†Electronic address: dimiter@unm.edu

still influence the capillary flow. Normal surface evaporation with capillary flow through porous media of constant cross section was first discussed in Fries *et al.* [21], and extended to 2D expanding geometries in Refs. [7, 13]. When the sides of the domain parallel to the flow and the normal surfaces are sealed off, the corresponding modes of evaporation cease; then if the far end of the domain is left open to the atmosphere, vapor loss may still occur through the wetting interface into the medium itself. This gives rise to the front evaporation effect. No prior experimental or theoretical work on front evaporation from 2D or 3D expanding flows in porous media is known.

Green–Ampt [22] theory describes the motion of the liquid into a porous medium by a discontinuous saturation profile [23]. In our Green–Ampt theory-based model, we assume the porous medium itself does not expand during wetting, the evaporation rate is constant, the process is isothermal, and viscous fingering instabilities may be ignored [24]. We quantify the effects of front evaporation on the rate of advancement of the wet front and the fluid uptake by the medium. In particular, we consider the onset of evaporation effects, where the Green–Ampt model is most relevant, and the evaporative steady state to understand how the evaporation comes to dominate the flow. Also, we compare the 2D normal surface evaporation effect found in Ref. [7] with our 2D front evaporation results to consider the relative asymptotic behaviors under given evaporation-capillary numbers.

The paper is organized as follows: In the next section, we outline the expressions of capillary wicking with mass loss by evaporation. Sec. III presents the derivations for the 2D and 3D expanding flows and other relevant solutions of capillary flow with evaporation. In Sec. IV we discuss effects of the front evaporation on the flow and variations in the flow behavior due to dimensionality. Finally, we summarize the conclusions in Sec. V.

II. GOVERNING EQUATIONS FOR CAPILLARY FLOW IN POROUS MEDIA WITH FRONT INTERFACE EVAPORATION

We incorporate evaporation through the wet front into the governing equations for the Lucas–Washburn method to analyze the effect on capillary wicking in porous media [8]. The potential flow formulation of the LW method begins with the conservation of mass equation in the liquid-filled portion of the domain,

$$\boldsymbol{\nabla}\cdot\mathbf{v} = -Q, \tag{1}$$

where the linear liquid velocity, $\mathbf{v}$, may be reduced through a given control volume by an evaporation loss, $Q > 0$, in that volume. In exposed thin porous media, we refer to this as normal surface evaporation, and this evaporation rate is the fractional mass loss rate given in units of inverse time.

Macroscale flow in porous media is irrotational [25], so the velocity may be given as the gradient of a velocity potential, φ;

$$\mathbf{v} = \boldsymbol{\nabla}\varphi. \tag{2}$$

Substituting into the conservation equation (1),

$$\nabla^2\varphi = -Q \tag{3}$$

for finite normal surface evaporation rates. When there is no evaporation loss through the normal surface, the conservation equation is simply $\boldsymbol{\nabla}\cdot\mathbf{v} = 0$, and we obtain

$$\nabla^2\varphi = 0 \tag{4}$$

for the velocity potential equation where the liquid-filled domain driven by capillary flow is affected only by front evaporation.

From the Darcy law, we may relate the internal pressure to the velocity potential, $\varphi = -kP/\mu$, where k is the permeability, μ is the viscosity, and P is the fluid pressure. Setting the velocity potential to zero at the front, the velocity potential at the inlet, φ_0, is then determined by the magnitude of the pressure change across the wetted regime, which is the capillary pressure, P_c, so $\varphi_0 = -kP_c/\mu$, when the effect of gravity via hydrostatic pressure is ignored. For the fully-saturated Green–Ampt flow model, the mass balance equation at the front interface may be expressed by equating the velocity of the actual front interface to the difference of the natural velocity in the liquid by capillary pressure minus the velocity reduction due to the evaporation, or

$$\frac{\mathrm{d}\mathbf{x}_f}{\mathrm{d}t} = \left[\boldsymbol{\nabla}\varphi\right|_{\mathbf{x}_f} - q_f\mathbf{n}_{\mathbf{x}_f}, \tag{5}$$

where $\mathbf{x}_f$ is the position of the front at time, t; q_f is the rate of loss through the front interface; and $\mathbf{n}_{\mathbf{x}_f}$ is the outward vector normal to the front interface. The side boundaries, $\mathbf{x}_s$, are insulated from the atmosphere, so there is no velocity flux, or $\left[\boldsymbol{\nabla}\varphi\right|_{\mathbf{x}_s}\cdot\mathbf{n}_{\mathbf{x}_s} = 0$. The rate of liquid entering the medium, U, which we also refer to as the bulk velocity, is the integral of the velocity through the inlet over the inlet cross-section;

$$U = -\iint_{\mathbf{x}_i}\left[\boldsymbol{\nabla}\varphi\right|_{\mathbf{x}_i}\cdot\mathbf{n}_{\mathbf{x}_i}\,\mathrm{d}\mathbf{x}_i. \tag{6}$$

III. CAPILLARY DRIVEN FLOW WITH EVAPORATION THROUGH VARIED INLET AND DOMAIN SHAPES

A. Expanding flow through a semicircular inlet with evaporation

Two-dimensional expanding flows in porous media are described most simply by polar coordinates as given by [26]

$$x = r\cos(\theta), \tag{7a}$$

$$y = r\sin(\theta). \tag{7b}$$

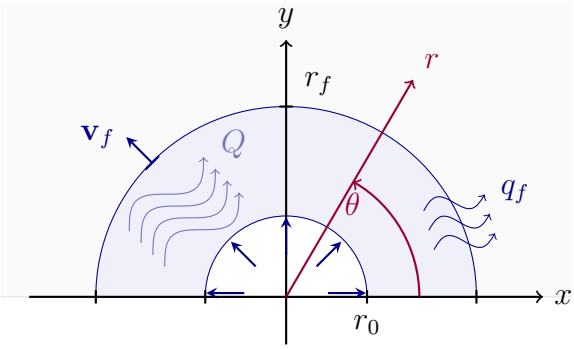

FIG. 1: Saturated capillary flow from a reservoir through a semicircular inlet of radius r_0 expanding two-dimensionally at velocity $\mathbf{v}_f$ into a dry porous domain described by polar coordinates as given in Eq. (7). Evaporation is occurring either through the wet *front interface* (located at r_f) at a rate of q_f or through the *normal surface* at rate Q when the porous medium is open to the air.

Figure 1 illustrates the coordinate system overlaying the wetting porous domain. The thickness of the porous medium in the z-direction, δ, is sufficiently small that we consider only behavior in the plane. The liquid enters the domain through a semicircular inlet of radius, r_0, and the domain is saturated with liquid out to the front radius, r_f. We first consider fluid being lost through the front by evaporation with a rate of q_f, but we will also briefly consider the case of evaporation through the normal surface with a rate of Q dominating the flow. This system only needs to be analyzed by changes in the variables along the line of the radial coordinate because the flow is not influenced in the angular direction by any other forces such as side evaporation or gravity.

1. *Front Interface Evaporation*

To consider the effect of front evaporation, per Eq. (4) the mass of the liquid is conserved within the wetted porous domain, and in polar coordinates. the radial Laplace equation is

$$\frac{\partial^2\varphi}{\partial r^2}+\frac{1}{r}\frac{\partial\varphi}{\partial r}=0. \tag{8}$$

The boundary conditions, $\varphi(r{=}r_0)=\varphi_0$ and $\varphi(r{=}r_f)=0$, account for the capillary force. The corresponding velocity potential is

$$\tilde{\varphi}=-\frac{\ln(\tilde{r}_f)-\ln(\tilde{r})}{\ln(\tilde{r}_f)}, \tag{9}$$

where the dimensionless variables are defined by $\tilde{\varphi}=(\mu/kP_c)\varphi$ and $\tilde{r}=r/r_0$. Using the expression $P=-\mu\varphi/k$, this equation is also equivalent to the negative of the dimensionless fluid pressure, $\tilde{P}=P/P_c$.

The internal liquid velocity in the radial direction is found from the derivative of the potential, Eq. (2),

$$\tilde{v}_r=\frac{1}{\tilde{r}}\frac{1}{\ln(\tilde{r}_f)}, \tag{10}$$

where the dimensionless velocity is $\tilde{v}=(\mu r_0/kP_c)v$. As defined in Eq. (5), substituting for the front radius and reducing the velocity by the front evaporation rate, we get the front velocity,

$$\tilde{v}_f=\frac{\mathrm{d}\tilde{r}_f}{\mathrm{d}\tilde{t}}=\frac{1}{\tilde{r}_f}\frac{1}{\ln(\tilde{r}_f)}-\mathfrak{N}_\mathrm{f}, \tag{11}$$

where $\tilde{t}=(kP_c/\mu r_0^2)t$. The last term is the dimensionless front evaporation rate and is a form of the evaporation-capillary number discussed in Ref. [7]. It is defined

$$\mathfrak{N}_\mathrm{f}=\frac{\mu r_0 q_f}{kP_c}, \tag{12}$$

where the subscript 'f' refers to the front interface. This dimensionless number is the ratio of the rate of evaporation to the characteristic rate of flow due to capillary wicking. We will usually refer to it simply as the evaporation number or as the front evaporation number in contrast to other quantities.

The equation for the front (11) may be put into integral form

$$\int_1^{\tilde{r}_f}\frac{\tilde{r}_f'\ln\left(\tilde{r}_f'\right)}{1-\mathfrak{N}_\mathrm{f}\tilde{r}_f'\ln\left(\tilde{r}_f'\right)}\,\mathrm{d}\tilde{r}_f'=\tilde{t}, \tag{13}$$

but the integral in the left hand side is not analytically tractable. However, to analyze the onset of front evaporation on the wicking rate, we may expand the integral to the first order evaporation term;

$$\begin{aligned}&\left[\frac{1}{2}\tilde{r}_f^2\ln(\tilde{r}_f)-\frac{\tilde{r}_f^2-1}{4}\right]\\&\quad+\mathfrak{N}_\mathrm{f}\left\{\frac{\tilde{r}_f^3\left[\ln(\tilde{r}_f)\right]^2}{3}-\frac{2\tilde{r}_f^3\ln(\tilde{r}_f)}{9}+\frac{2(\tilde{r}_f^3-1)}{27}\right\}\\&\quad+\mathcal{O}\left({\mathfrak{N}_\mathrm{f}}^2\tilde{r}_f^4\left[\ln(\tilde{r}_f)\right]^3\right)=\tilde{t}.\end{aligned} \tag{14}$$

In the absence of evaporation, or $\mathfrak{N}_\mathrm{f}=0$, Eq. (14) reduces to the known relation of 2D radial capillary flow as given by equation (7) in Hyväluoma *et al.* [17]. For small values of the evaporation number, the highest order terms in the radius will come to dominate the asymptotic behavior, and we may simplify to

$$\frac{1}{2}\tilde{r}_f^2\ln(\tilde{r}_f)+\frac{1}{3}\mathfrak{N}_\mathrm{f}\tilde{r}_f^3\left[\ln(\tilde{r}_f)\right]^2\approx\tilde{t}. \tag{15}$$

Conversely, for the steady state induced by the evaporation, indicated by the 'ss' subscript, the front velocity equation (11) reduces to

$$\tilde{r}_{f,\,\mathrm{ss}}\ln(\tilde{r}_{f,\,\mathrm{ss}})=1/\mathfrak{N}_\mathrm{f}, \tag{16}$$

wherein the front evaporation fully dominates the system.

Substituting the velocity at the inlet determined from Eq. (10) into Eq. (6), we find the dimensionless bulk velocity is

$$\tilde{U} = \frac{\pi}{\ln(\tilde{r}_f)}, \tag{17}$$

where $\tilde{U} = (\mu/kP_c\delta)U$. This is valid for front evaporation because that effect is accounted for by the front velocity equation only and therefore does not directly affect the bulk velocity.

2. *Normal Surface Evaporation*

In the results, we will compare the time-dependent behavior of front evaporation with normal surface evaporation to consider distinctions in their phenomenological manifestations. The model of two-dimensional capillary flow with normal evaporation was first derived by Liu, *et al.* [13] and was advanced in Ref. [7] where the results were presented in a dimensionless formulation. In the process of non-dimensionalizing the system, the normal surface evaporation-capillary number was shown to be

$$\mathfrak{N}_{\rm n} = \frac{\mu r_0^2 Q}{kP_c}, \tag{18}$$

where the 'n' subscript indicates the quantity is specifically for the normal surface.

When a physical system includes both front and normal surface evaporation, the normal surface evaporation number, $\mathfrak{N}_{\rm n}$, will be significantly greater than the front evaporation number, $\mathfrak{N}_{\rm f}$. This arises from the fact that $\delta Q > q_f$ because q_f is into the porous medium, so $\mathfrak{N}_{\rm n} > (r_0/\delta)\mathfrak{N}_{\rm f}$. Furthermore, the aspect ratio is assumed to be large, so for a thin system that includes both effects $\mathfrak{N}_{\rm n} > \mathfrak{N}_{\rm f}$. For this reason, we primarily compare the two evaporation effects asymptotically.

By solving Eq. (3), the implicit analytical solution for the front position with time was given in equation (12) of Ref. [7]:

$$\ln\left\{1 - \frac{1}{4}\mathfrak{N}_{\rm n}\left[\tilde{r}_f^2\ln\left(\tilde{r}_f^2\right) - \left(\tilde{r}_f^2 - 1\right)\right]\right\} = -\mathfrak{N}_{\rm n}\tilde{t}, \tag{19}$$

Similar to Eq. (13), asymptotics were derived for the front position equation in Ref. [7] which will be revisited in this paper.

B. Expanding flow through a hemispherical inlet with front evaporation

We next consider a porous medium of a half-space domain with a hemispherical inlet of radius r_0, as shown in Fig. 2, which is the simplest example of 3D flow. This

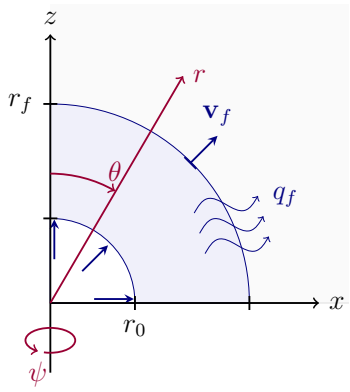

FIG. 2: Three-dimensionally expanding wicking from a hemispherical inlet into a dry porous domain with front evaporation loss, q_f, described by spherical coordinates given in Eq. (20). The volume is rotated symmetrically around the z-axis.

system is described by spherical coordinates as defined by [26]

$$x = r\sin(\theta)\cos(\psi), \tag{20a}$$
$$y = r\sin(\theta)\sin(\psi), \tag{20b}$$
$$z = r\cos(\theta). \tag{20c}$$

Evaporation again occurs through the front at a rate q_f, where the capillary force is driving the fluid motion and the two phenomena are only affecting the flow along the local radial direction.

The spherical Laplace equation for the velocity potential within the wetted region is

$$\frac{\partial^2\varphi}{\partial r^2} + \frac{2}{r}\frac{\partial\varphi}{\partial r} = 0, \tag{21}$$

and the capillary boundary conditions are $\varphi(r{=}r_0) = \varphi_0$ and $\varphi(r{=}r_f) = 0$. The resulting velocity potential is

$$\tilde{\varphi} = -\frac{\tilde{r}_f - \tilde{r}}{\tilde{r}_f - 1}\frac{1}{\tilde{r}}. \tag{22}$$

Differentiating the potential, the velocity in the radial direction is

$$\tilde{v}_r = \left(\frac{\tilde{r}_f}{\tilde{r}_f - 1}\right)\frac{1}{\tilde{r}^2}. \tag{23}$$

When we again include the front evaporation effect, Eq. (5), the front velocity is

$$\tilde{v}_f = \frac{1}{\tilde{r}_f^2 - \tilde{r}_f} - \mathfrak{N}_{\rm f}. \tag{24}$$

In integral form,

$$\int_1^{\tilde{r}_f} \frac{\tilde{r}_f'^2 - \tilde{r}_f'}{1 - \mathfrak{N}_{\rm f}(\tilde{r}_f'^2 - \tilde{r}_f')}\,{\rm d}\tilde{r}_f' = \tilde{t}. \tag{25}$$

Expanding the integral in powers of $\tilde{r}_f$ and $\mathfrak{N}_\mathrm{f}$, we find,

$$\left(\frac{\tilde{r}_f^3}{3}-\frac{\tilde{r}_f^2}{2}+\frac{1}{6}\right)+\mathfrak{N}_\mathrm{f}\left(\frac{\tilde{r}_f^5}{5}-\frac{\tilde{r}_f^4}{2}+\frac{\tilde{r}_f^3}{3}-\frac{1}{30}\right) + \mathcal{O}\big({\mathfrak{N}_\mathrm{f}}^2\tilde{r}_f^7\big)=\tilde{t}. \tag{26}$$

Without evaporation, this reduces to the implicit relation for 3D capillary flow given in equation (8) of Xiao *et al.* [18]. The early-time, first-order perturbation effect of the front evaporation for small $\mathfrak{N}_\mathrm{f}$ is

$$\frac{1}{3}\tilde{r}_f^3+\frac{1}{5}\mathfrak{N}_\mathrm{f}\tilde{r}_f^5\approx\tilde{t}. \tag{27}$$

From Eq. (24), we find the front evaporation steady state is

$$\tilde{r}_{f,\,\mathrm{ss}}^2-\tilde{r}_{f,\,\mathrm{ss}}=1/\mathfrak{N}_\mathrm{f}, \tag{28}$$

so for 3D flows with $\mathfrak{N}_\mathrm{f}\ll 1$, $\tilde{r}_{f,\,\mathrm{ss}}\approx 1/\sqrt{\mathfrak{N}_\mathrm{f}}$.

Unlike with the front velocity equation in polar coordinates, the integral in Eq. (25) is analytically tractable, and the implicit solution for the capillary flow with front evaporation is

$$\frac{2}{\sqrt{4/\mathfrak{N}_\mathrm{f}+1}}\left[\tanh^{-1}\left(\frac{1}{\sqrt{4/\mathfrak{N}_\mathrm{f}+1}}\right) -\tanh^{-1}\left(\frac{2\tilde{r}_f-1}{\sqrt{4/\mathfrak{N}_\mathrm{f}+1}}\right)\right]+\mathfrak{N}_\mathrm{f}\left(\tilde{r}_f-1\right)=-{\mathfrak{N}_\mathrm{f}}^2\tilde{t}. \tag{29}$$

Expanding Eq. (29) in powers of $\mathfrak{N}_\mathrm{f}$ yields the identical series given in Eq. (26). Also, when the term within the parenthesis of the second $\tanh^{-1}$ function is set to one, we recover Eq. (28), which indicates that the solution will correctly approach the asymptotic limit of the steady-state.

The bulk velocity is determined from the radial velocity at the inlet and Eq. (6) via $\tilde{U}=(1/\tilde{\delta})\int_0^{2\pi}\mathrm{d}\psi\int_0^{\pi/2}\tilde{r}_f/(\tilde{r}_f-1)\sin(\theta)\,\mathrm{d}\theta$ and simplifies to

$$\tilde{U}=\frac{2\pi}{\tilde{\delta}}\frac{\tilde{r}_f}{\tilde{r}_f-1}. \tag{30}$$

The aspect ratio of the thin planar domain, $1/\tilde{\delta}=r_0/\delta$, arises for this 3D case due to the change in inlet shape from flat to hemispherical through the original definition of the bulk velocity. For a steady state with $\mathfrak{N}_\mathrm{f}\ll 1$, the bulk velocity is $\tilde{U}_\mathrm{ss}\approx(2\pi/\tilde{\delta})(1+\sqrt{\mathfrak{N}_\mathrm{f}})$. Here we observe again the finite capillary steady state of the three-dimensional system [1, 18].

C. Flow through a medium of constant cross-section with evaporation

Before proceeding to analyze the solutions for two- and three-dimensional flow, we must review the prior results for capillary flow in one-dimension with evaporation to facilitate comparison amongst all three geometries. We refer to this as the 1D flow or the 1D geometry to distinguish it from the 2D and 3D cases above.

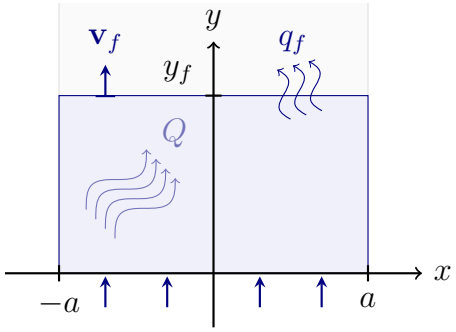

FIG. 3: Wicking through a medium of constant cross-section into a dry porous domain with front evaporation, q_f, or normal surface evaporation, Q.

The effects of normal surface and front evaporation on capillary flow through a rectangular constant cross-sectional porous medium were covered in Ref. [8]. Figure 3 illustrates the geometry for the two systems, where the effects of each form of evaporation is considered separately. The porous medium maps onto standard Cartesian coordinates, where the inlet has width $2a$ along the x-axis, the front is moving in the positive y-direction, and the front position is denoted by y_f.

1. *Front Interface Evaporation*

The front position equation for 1D capillary flow with front evaporation may be derived by the same procedure as above, and is given by equation (46) of Ref. [8];

$$\mathfrak{N}_\mathrm{f}\tilde{y}_f+\ln\left|1-\mathfrak{N}_\mathrm{f}\tilde{y}_f\right|=-{\mathfrak{N}_\mathrm{f}}^2\tilde{t}. \tag{31}$$

Incidentally, this solution is identical in form to the equation of capillary rise against restraining gravity. Similar to Eq. (29), the steady-state is reached when the terms in the logarithm equal zero (the function singularity), and so

$$\tilde{y}_{f,\mathrm{ss}}=1/\mathfrak{N}_\mathrm{f}, \tag{32}$$

which constitutes an evaporative analogue to the Jurin height [6]. (See also equations (37) and (54) in Ref. [8].)

As we have discussed with Eq. (17), the bulk velocity does not explicitly include the front evaporation and is thus the simple 1D capillary flow bulk velocity,

$$\tilde{U}=\frac{2}{\tilde{y}_f}; \tag{33}$$

this is shown with equation (49) of Ref. [8].

2. Normal Surface Evaporation

The 1D normal surface evaporation solution was first given in Fries, *et al.* [21] which additionally included restraint by gravity. Their solution reduces to

$$\ln\left(1-\frac{1}{2}\mathfrak{N}_{\mathrm{n}}\tilde{y}_f^2\right)=-\mathfrak{N}_{\mathrm{n}}\tilde{t}, \tag{34}$$

which may also be derived from Eq. (3) as shown by equation (31) of Ref. [8]. Finally, the steady-state front position is given by $\tilde{y}_{f,\mathrm{ss}}=\sqrt{2/\mathfrak{N}_{\mathrm{n}}}$.

IV. RESULTS AND DISCUSSION

A. Time dependence of penetration length in the presence of front evaporation

Figure 4 shows the position of the front with time, or the front behavior, for capillary flows with front evaporation. The front position for the 2D radially-expanding flow given by Eq. (11) is shown in Fig. 4a, where the evaporation causes the advancement to decrease to a steady state for all values of $\mathfrak{N}_{\mathrm{f}}$. Furthermore, the 2D front expansion without evaporation ($\mathfrak{N}_{\mathrm{n}}=0$) advances very nearly in the shape of a sideways parabola; only a logarithmic deviation is expected as indicated in Eq. (11). In Fig. 4b we observe that for the 3D expanding flow given by Eq. (24) the front does not penetrate as deeply as the 2D case. Furthermore, the front does not significantly advance beyond the inlet unless $\mathfrak{N}_{\mathrm{f}}<1$. At the limit of no evaporation, $\mathfrak{N}_{\mathrm{n}}=0$, the front position function conforms to the inverse cubic dependence on time, $\tilde{r}_f\sim\sqrt[3]{\tilde{t}}$, as predicted in Eq. (27).

Figure 5 compares the time dependent behavior of the expanding 2D front similar to Fig. 4a but with varying evaporation numbers for both front and normal surface evaporation. The front evaporation is computed via Eq. (11), and the normal surface is determined by Eq. (19), then both are plotted in logarithmic form. To consider the real distance the front has moved from the inlet instead of from the origin of the coordinate system, we define the front penetration length, $\Delta\tilde{r}_f=\tilde{r}_f-1$, as the new variable from which we consider motion of the front. The unity term comes from the dimensionless inlet radius, $\tilde{r}_0=1$. This is particularly useful for comparing the motions of the fronts at early times, where the higher dimensions may be asymptotically similar to one-dimensional flow.

We observe in Fig. 5 significant distinctions between front and normal surface evaporation as to when the evaporation begins to clearly influence the flow. For high evaporation numbers, $\mathfrak{N}_{\mathrm{f}}=\mathfrak{N}_{\mathrm{n}}>1$, the front evaporation begins to influence the flow sooner and reaches a steady state earlier than normal surface evaporation. The reverse occurs for low evaporation numbers, $\mathfrak{N}_{\mathrm{f}}=\mathfrak{N}_{\mathrm{n}}\ll 1$.

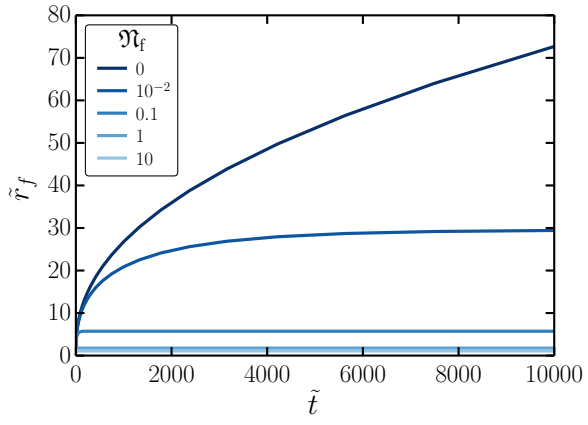

(a)

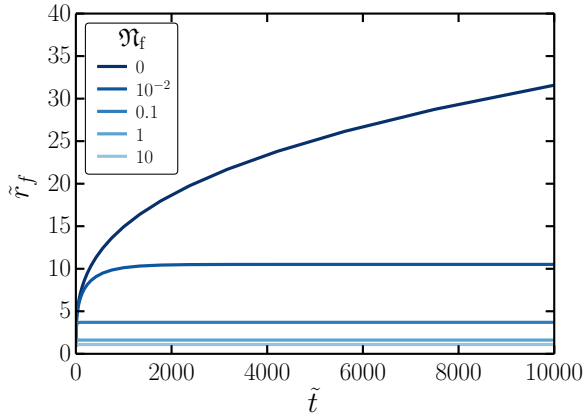

(b)

FIG. 4: Front position, $\tilde{r}_f$, versus time, $\tilde{t}$, for varying evaporation number, $\mathfrak{N}_{\mathrm{f}}$. (a) 2D flow through circular inlet described by polar coordinates in Figure 1. (b) 3D flow through hemispherical inlet described by spherical coordinates in Figure 2.

Let's first consider the onset of the evaporation effect for the early times and high evaporation numbers, illustrated by $\mathfrak{N}_{\mathrm{f}}=\mathfrak{N}_{\mathrm{n}}=10$, and analytically contrast the front evaporation effect with that of the normal surface evaporation. The two-dimensional expanding geometry of the flow does not have a significant effect when the propagation has advanced much less than the inlet size, so in this regime, we may consider the simpler one-dimensional solutions.

In the 1D-like geometry, or a medium of constant cross-section, the $\tilde{y}_f$ variable is also the front penetration length. The simplest relation of 1D capillary flow, the Lucas–Washburn equation, indicates the front position is proportional to the square root of the time, or $\tilde{y}_f^2\sim\tilde{t}$. The asymptotic relation for the onset of the front evaporation effect on 1D capillary flow may be derived

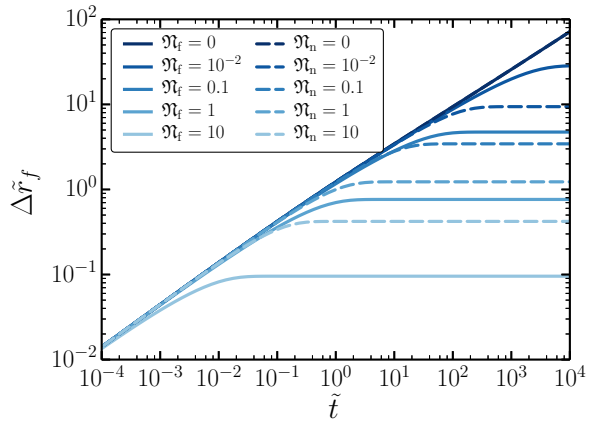

FIG. 5: Logarithmic comparison of the front penetration length, $\Delta\tilde{r}_f$, with time, $\tilde{t}$, for 2D expanding flows between front and normal evaporation effects by varying values of the front evaporation number, $\mathfrak{N}_\mathrm{f}$, and the normal surface evaporation number, $\mathfrak{N}_\mathrm{n}$.

by expanding Eq. (31);

$$\frac{1}{2}\tilde{y}_f^2\left(1+\frac{2}{3}\mathfrak{N}_\mathrm{f}\,\tilde{y}_f\right)\approx\tilde{t}. \tag{35}$$

In effect, this shows how the front advancement rate begins to deviate from the LW equation. The first-order term for the front evaporation is technically cubic in the front length, and therefore deviates from the ideal by the front length to the first power. However, when we consider the asymptotic relation for the normal surface evaporation, the first-order evaporation term for the front length is quintic,

$$\frac{1}{2}\tilde{y}_f^2\left(1+\frac{1}{4}\mathfrak{N}_\mathrm{n}\,\tilde{y}_f^2\right)\approx\tilde{t}, \tag{36}$$

and so the deviation from LW is determined by the length to the *second* power. This expression is given in equation (38) of Ref. [7] as an expansion of Eq. (34). From the coefficients and the exponents of the evaporation terms, we ascertain that the front evaporation will have stronger deviations from capillary flow (the LW Eq.) sooner than normal evaporation for $\mathfrak{N} \geq 1$. For low evaporation numbers, however, due to the higher-order spatial effect of the normal surface evaporation, it both onsets sooner and more rapidly than for front evaporation, as we observe in Fig. 5.

Physically, this difference is due to the surface area through which the front evaporation occurs not changing as the front position advances (effectively zero-dimensional behavior), while the surface area for normal surface evaporation is growing linearly (1D-like behavior). Thus, normal evaporation progressively gains a larger surface area for evaporation to occur and through which the mass lost per time increases, while the the mass loss from the liquid phase due to front evaporation is a constant.

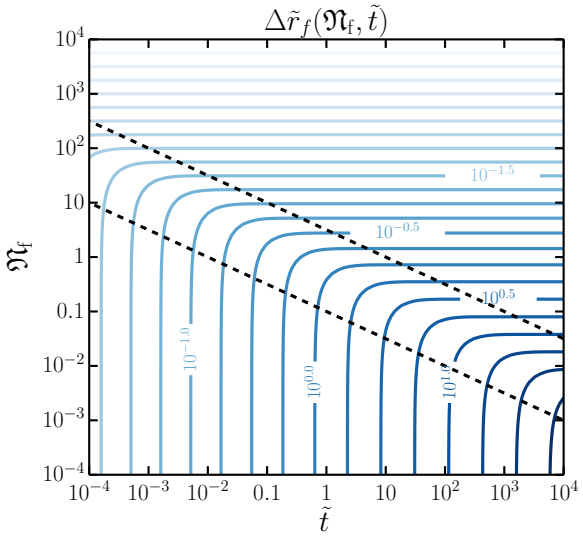

(a)

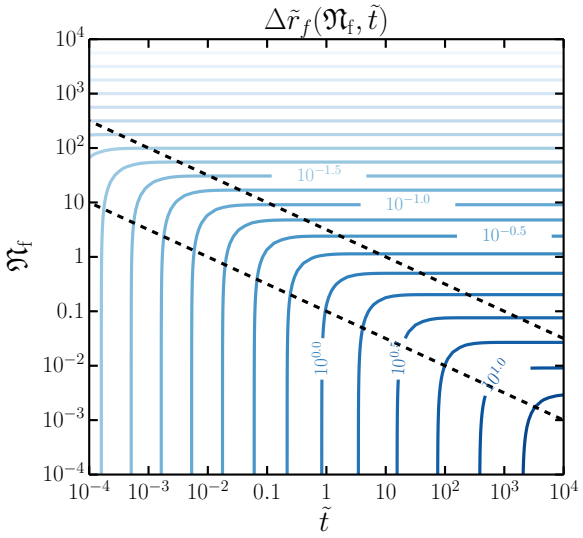

(b)

FIG. 6: Contour plot of front penetration length, $\Delta\tilde{r}_f$, over evaporation number, $\mathfrak{N}_\mathrm{f}$, and time, $\tilde{t}$. Dashed black lines in the lower left and upper right of each figure correspond to ${\mathfrak{N}_\mathrm{f}}^2\tilde{t} = 0.01$ and ${\mathfrak{N}_\mathrm{f}}^2\tilde{t} = 10$, respectively. The lower left section is primarily dominated by the capillary flow, and the upper right has reached evaporative steady state. (a) 2D flow through circular inlet. (b) 3D flow through hemispherical inlet.

To visualize the onset of the initial evaporation effect and the steady state, Figure 6 presents contours of the front penetration length as a function of both evaporation number and time. These figures are computed from Eqs. (11) and (24) for the 2D and 3D radial expansions,

respectively. The lines of $\mathfrak{N}_\mathrm{f}{}^2\tilde{t} = 0.01$ and $\mathfrak{N}_\mathrm{f}{}^2\tilde{t} = 10$ are shown to indicate the approximate separation of the regimes of the flow behavior between capillary dominated flow, evaporative steady state, and the coupled transition of evaporation-influenced capillary-driven motion. This stems from the time portion of the solutions being most naturally expressed with $\mathfrak{N}_\mathrm{f}{}^2\tilde{t}$ in the general solutions for the front motion as illustrated in the right hand sides of Eqs. (31) and (29) for 1D and 3D geometries, respectively. This is in contrast to normal surface evaporation, where the phenomenology is constrained by the direct product of the evaporation number and time, $\mathfrak{N}_\mathrm{n}\tilde{t}$, as suggested in Eqs. (34) and (19) for the 1D and 2D geometries, respectively. This nature of the time scale of effects of normal surface evaporation is further detailed in Refs. [8] and [7]. Thus, we find that the product $\mathfrak{N}_\mathrm{f}{}^2\tilde{t}$ renders an easy estimate of the flow dominance of the front evaporation effect on the capillary flow.

Figure 6a shows the flow behavior regimes for the wicking into a 2D expansion with front evaporation. At high evaporation numbers, the values are consistent with the purely 1D flow case as we noted above, where both the onset of evaporation and the end of the front motion are governed by the product, $\mathfrak{N}_\mathrm{f}{}^2\tilde{t}$. As derived in Eq. (15) for 2D radial expansion, the lowest order effect of the evaporation, and highest order effect in space for capillary flow (which is dominant for large expansions), is described by

$$\frac{1}{2}\tilde{r}_f^2\ln(\tilde{r}_f)\left[1+\frac{2}{3}\mathfrak{N}_\mathrm{f}\,\tilde{r}_f\ln(\tilde{r}_f)\right]\approx\tilde{t}. \tag{37}$$

As was the case for 1D evaporation, the lowest-order evaporation effect on the front length by the front evaporation—the $\tilde{r}_f\ln(\tilde{r}_f)$ term—differs from normal surface evaporation by being one polynomial order less $[\tilde{r}_f^2\ln(\tilde{r}_f)]$, as we see in

$$\frac{1}{2}\tilde{r}_f^2\ln(\tilde{r}_f)\left[1+\frac{1}{4}\mathfrak{N}_\mathrm{n}\,\tilde{r}_f^2\ln(\tilde{r}_f)\right]\approx\tilde{t}, \tag{38}$$

which may be derived from Eq. (19) as shown with equation (39) of Ref. [7]. Thus, between each of the 1D and 2D cases, it appears that the first-order evaporation term is one polynomial order lower for the front evaporation than for the normal evaporation.

Also, like with the 1D case, this may be physically reflective of the fact that the surface area through which the front evaporation occurs is only growing linearly (1D-like) with the front advancement, while for the normal evaporation, the area is growing quadratically (2D-like). In regards to the geometry, this means the front evaporation generally begins to affect the flow sooner for 2D than for 1D expansions, and the steady state is reached a little more rapidly in the 2D expanding flow domains.

In Figure 6b we plot the contours of the front penetration for the 3D spherical expansion. First, recall Eq. (27), which gives the power law for 3D radial capillary flow with front evaporation;

$$\frac{1}{3}\tilde{r}_f^3\left(1+\frac{3}{5}\mathfrak{N}_\mathrm{f}\,\tilde{r}_f^2\right)\approx\tilde{t}. \tag{39}$$

In the figure, we notice stronger differences in the lower evaporation and long-time regime of the flow (the bottom right corner). The vertical contour lines indicating the capillarity-dominated regime are more spread out due to the slower advancement of the front in the large time limit, as suggested analytically by the $\tilde{r}_f^3$ term, which is higher-order than the capillary terms for both 1D and 2D flows, as shown in Eqs. (35) and (37), respectively. This results in the nearly-vertical contour lines contacting $\mathfrak{N}_\mathrm{f}{}^2\tilde{t} = 0.01$ already having begun to curve before reaching the dashes. Such deviations indicate the evaporation effect has already set in, and also for this parameter region of the 3D system, $\mathfrak{N}_\mathrm{f}{}^2\tilde{t}$ does not accurately predict the transition region from capillary-driven flow to evaporation steady state. We observe that the lowest-order evaporation term deviates from the dominant capillary term by $\tilde{r}_f^2$, whereas it only differed linearly, $\tilde{r}_f$, for the 1D case. This contributes to the stronger low-$\mathfrak{N}_\mathrm{f}$ evaporation effect onset from the 1D-like flow and suggests that for 3D expanding flows with a very low front evaporation number, the evaporation transition regime is determined by $\mathfrak{N}_\mathrm{f}{}^n\tilde{t}$ with $n < 2$. Finally, the surface area of the interface through which the front evaporation occurs is now growing for 3D expansions quadratically (2D-like), so the evaporation rapidly becomes more significant as the front advances.

B. Rate of liquid absorption

We consider the flow rate into the porous medium as a function of time with varying evaporation numbers in Figure 7. Here and for all later figures, the bulk velocity is normalized to the same inlet area for all dimensionalities so that the bulk velocity relations are comparable at early-time and high evaporation number asymptotics. The new normalized bulk velocities are defined for each dimensionality by $\tilde{U}^*_\mathrm{1D} = \tilde{U}/2$ for flow in a medium of constant cross section; $\tilde{U}^*_\mathrm{2D} = \tilde{U}/\pi$ for flow through a circular inlet into a thin half-plane; and $\tilde{U}^*_\mathrm{3D} = (\tilde{\delta}/2\pi)\tilde{U}$ for flow through a hemispherical inlet into a half-space.

Using Eq. (17), the 2D bulk velocity behavior is shown in Fig. 7a, where we see the flow deviates from the 1D inflow rate after dimensionless times greater than unity. In addition to the capillarity and dimensionality, the evaporation determines the magnitude of the bulk velocity, resulting in a higher steady state value. In Fig. 7b, where the 3D bulk velocity given by Eq. (30) is plotted for varying $\mathfrak{N}_\mathrm{f}$, we see the usual finite steady state for pure capillary flow [1] which causes the evaporation to have a nearly negligible affect on the bulk velocity for $\mathfrak{N}_\mathrm{f} < 0.01$. For high values of $\mathfrak{N}_\mathrm{f}$, the normalized bulk velocity is slightly greater than for the 1D and 2D geometries.

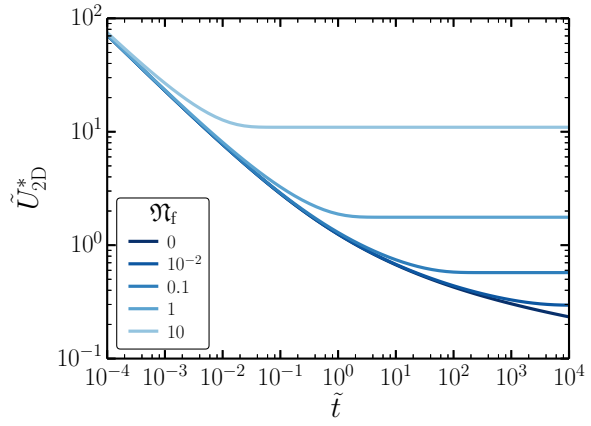

(a)

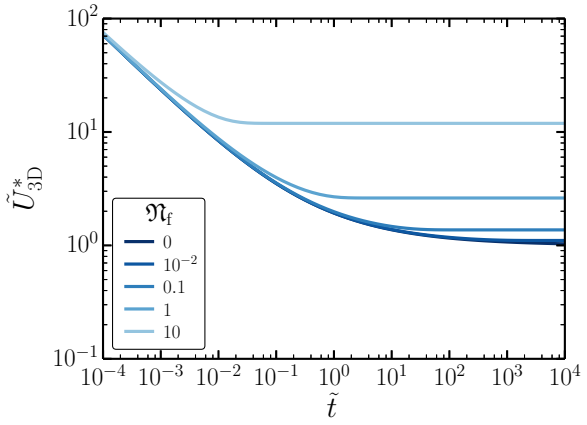

(b)

FIG. 7: Inlet-normalized bulk velocity, $\tilde{U}^*$, versus time, $\tilde{t}$, for expanding flows with evaporation from the front. Liquid absorption rate through (a) 2D semicircular inlet and (b) 3D hemispherical inlet.

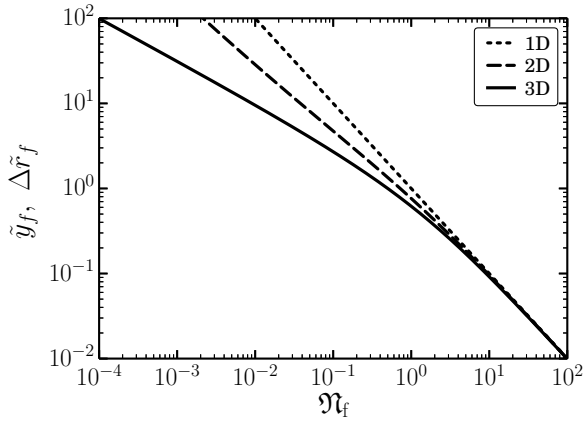

(a)

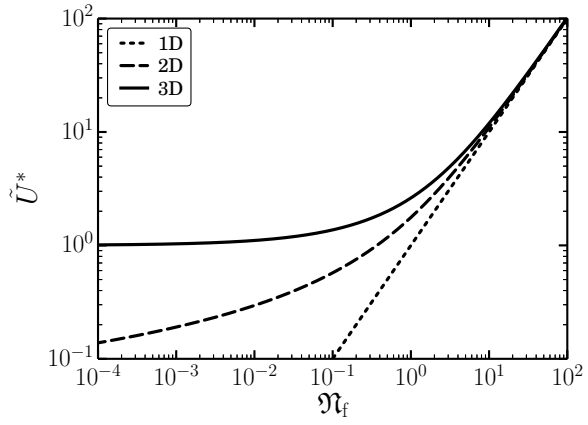

(b)

FIG. 8: Steady state variation of front penetration and bulk velocity with dimensionality over $\mathfrak{N}_f$. Dimensionalities are represented by wetting porous domains of constant cross section (1D), circular inlet into half-plane (2D), and hemispherical inlet into half-space (3D). (a) Front penetration length vs. evaporation number. (b) Inlet-normalized bulk velocity vs. evaporation number. Bulk velocity is normalized for all inlet sizes.

C. Front evaporation steady states for varying expansion dimensionality

As we have observed with sufficiently long times, the capillary flow reaches a steady state due to the front evaporation; Figure 8 plots the magnitude of the steady state variables as a function of the evaporation number. In Figure 8a, we see the evaporative steady state in a constant cross-sectional medium (*i.e.* 1D) is determined trivially by

$$\tilde{y}_{f,\mathrm{ss}} = 1/\mathfrak{N}_\mathrm{f}, \tag{40}$$

as given in Eq. (32). In other words, for wicking in 1D domains the steady state front position simply equals the inverse of the front evaporation number. In the 2D system, the steady state front position is given implicitly in Eq. (16) which may be formulated as

$$(\Delta\tilde{r}_{f,\mathrm{ss}} + 1)\ln(\Delta\tilde{r}_{f,\mathrm{ss}} + 1) = 1/\mathfrak{N}_\mathrm{f}. \tag{41}$$

For high evaporation numbers, we may expand the left hand side; $\Delta\tilde{r}_{f,\mathrm{ss}} + \Delta\tilde{r}^2_{f,\mathrm{ss}}/2 \approx 1/\mathfrak{N}_\mathrm{f}$, which also matches the 1D case since $\Delta\tilde{r}_{f,\mathrm{ss}} < 1$ in this region. In the low evaporation region, the 2D steady state deviates from the 1D as the $\ln(\Delta\tilde{r}_{f,\mathrm{ss}} + 1)$ term grows with increasing $\Delta\tilde{r}_{f,\mathrm{ss}}$.

As shown in Figure 8a in the low evaporation limit, the deviation of 3D flow from the 1D steady state front position is related approximately to the inverse square root of the evaporation number for small values of $\mathfrak{N}_\mathrm{f}$, or $\Delta\tilde{r}_{f,\mathrm{ss}} \sim 1/\sqrt{\mathfrak{N}_\mathrm{f}}$. This was predicted by Eq. (28), which

exactly reformulates in terms of the front penetration length to

$$\Delta\tilde{r}_{f,\,\mathrm{ss}}^{2} + \Delta\tilde{r}_{f,\,\mathrm{ss}} = 1/\mathfrak{N}_{\mathrm{f}} \tag{42}$$

for all evaporation numbers. This relation clearly gives the observed 1D-like behavior with high evaporation numbers for 3D flows. Furthermore, this suggests that for small to intermediate length expansions ($\Delta\tilde{r}_{f,\,\mathrm{ss}} \leq 1$ in Figure 8a) the quadratic term for the 3D case is nearly twice that of the 2D case. So the steady-state front penetration the 3D case deviates increasingly from the 1D case by about twice as much as the 2D case for high evaporation numbers.

Figure 8b shows the steady state bulk velocity versus the evaporation number for flows of each dimensionality. From Eqs. (32) and (33), the bulk velocity for 1D steady state front evaporation in inlet normalized notation is

$$\tilde{U}^{*}_{\mathrm{1D,ss}} = \mathfrak{N}_{\mathrm{f}}, \tag{43}$$

which matches the trend observed in the figure. The 2D steady state bulk velocity cannot be expressed by transcendental functions for the low evaporation number asymptotics due to the non-invertible $\tilde{r}_f \ln(\tilde{r}_f)$ term in the steady state front position. We see the 2D trend deviates from the 1D with a significantly greater steady state for $\mathfrak{N}_{\mathrm{f}} < 1$. From Eq. (30), $\tilde{U}_{\mathrm{ss}}$ for the 3D geometry goes to a constant with respect to $\mathfrak{N}_{\mathrm{f}}$ due to the 3D intrinsic finite capillary steady state. For finite $\mathfrak{N}_{\mathrm{f}}$ less than 0.1, this asymptotic behavior is

$$\tilde{U}^{*}_{\mathrm{3D,ss}} \approx 1 + \sqrt{\mathfrak{N}_{\mathrm{f}}}. \tag{44}$$

This deviation brought by the evaporation number is small in the low evaporation number region of Fig. 8b. Thus, for the 3D domains, front evaporation does not significantly increase the flow rate through the inlet relative to the intrinsic flow due to the geometry itself.

V. CONCLUSIONS

Front evaporation affects the behavior of capillary flows in two- and three-dimensional porous domains in distinct ways from normal surface evaporation. We have shown that for small evaporation numbers and large expansions the evaporation onset on the 2D front behavior may be implicitly approximated with the truncated power series $\tilde{r}_f^2 \ln(\tilde{r}_f) + 2\mathfrak{N}_{\mathrm{f}}\tilde{r}_f^3[\ln(\tilde{r}_f)]^2/3 \sim \tilde{t}$, and for the 3D case, the power series is $\tilde{r}_f^3 + 3\mathfrak{N}_{\mathrm{f}}\tilde{r}_f^5/5 \sim \tilde{t}$. The first-order affect of the evaporation in each front position power series for front evaporation are one polynomial order less than the equivalent power series for normal surface evaporation, which indicates the normal evaporation affect is stronger for small values of the two evaporation numbers, $\mathfrak{N}_{\mathrm{f}}$ and $\mathfrak{N}_{\mathrm{n}}$. Conversely for large evaporation numbers, the front evaporation affects the flow at an earlier time than normal evaporation. These power series also indicate that front evaporation affects the front motion sooner for 3D than 2D geometry.

Generally, the onset of the evaporation effect from capillary flow—the flow transition region—for front evaporation is governed by the product of the evaporation number squared and the time; ${\mathfrak{N}_{\mathrm{f}}}^2\tilde{t}$, unlike the normal surface evaporation where the transition region is governed by $\mathfrak{N}_{\mathrm{n}}$ to the first power. As an estimate of the regions of phenomenological dominance, when the dimensionless time has become greater than $10/{\mathfrak{N}_{\mathrm{f}}}^2$ the system will have reached evaporative steady state. Similarly, for flow analysis timescales about three orders of magnitude smaller or less, the process remains dominated by capillary flow. However, for very low evaporation numbers some deviation occurs in the 2D, and more noticeably the 3D, expansions such that the evaporation influences the flow earlier than this estimate.

Finally, we showed the high accuracy of given power laws approximating the steady state dependance of front length and bulk velocity as a function of the evaporation number. While in the steady state the front penetration is proportional to the inverse evaporation number, $\tilde{y}_{f,\mathrm{ss}} = 1/\mathfrak{N}_{\mathrm{f}}$, for the 1D flow, it deviates to $\Delta\tilde{r}_{f,\,\mathrm{ss}} \approx 1/\sqrt{\mathfrak{N}_{\mathrm{f}}}$ for small evaporation numbers with 3D flow. The steady state net liquid flow rate into the medium is directly proportional to the front evaporation number for 1D flows, $\tilde{U}^{*}_{\mathrm{1D,ss}} = \mathfrak{N}_{\mathrm{f}}$. However, the 3D bulk flow goes quickly to the 3D geometric steady state with a deviation by the square root of the evaporation number in the low evaporation limit, or $\tilde{U}^{*}_{\mathrm{3D,ss}} \approx 1 + \sqrt{\mathfrak{N}_{\mathrm{f}}}$, which highlights the necessity of accounting for the 3D geometry in steady-state analysis with front evaporation.

Further work remains in the development of the theory of front evaporation affects on capillary wicking. To the authors' knowledge, no published experiments have been conducted on either of the systems analyzed in this paper. In particular, the front evaporation rate versus saturation relation is unknown and should be determined empirically before further theory or computation may be done. Earth's gravity is also a likely technical challenge to experiments due to the significant deformation of the front shape which gravity may cause before the front evaporation measurably influences the flow. Furthermore, capillary condensation in the porous medium may diffuse the wetting front such that Green–Ampt theory may hold for a limited time under such front evaporation [16, 27]. Thus, the phenomenon of front evaporation during wicking should be further investigated through the framework of partially saturated capillary wetting via Richards equation coupled with a Brooks–Corey model to accommodate the great variety of empirically observed diffuse wetting fronts and general saturation profiles [23, 28]. This future analysis may be carried out by continuum simulations of partially saturated flow or three-dimensional pore-scale computational models of two phase flow.

Acknowledgments

This work was funded by grants from the NSF (CBET 0844645) and the Air Force Academy under cooperative agreement No. FA7000-14-2-0017 through funding from the Corrosion Policy and Oversight office, and the United States Department of Energy, Office of Basic Energy Sciences, Division of Materials Sciences and Engineering.

[1] E. M. Benner and D. N. Petsev, Phys. Rev. E **87**, 033008 (2013).
[2] M. Prat, Chemical engineering journal **86**, 153 (2002).
[3] M. Sadeghi, N. Shokri, and S. B. Jones, Water Resources Research **48** (2012).
[4] J. R. Philip, in *Water in the Unsaturated Zone, Proceedings of the Wageningen Symposium* (1966), vol. 1, pp. 503–516.
[5] M. Liu, J. Wu, Y. Gan, D. A. H. Hanaor, and C. C. Q., Int. J. Heat and Mass Trans. **123**, 239 (2018).
[6] J. Xiao, J. Cai, and J. Xu, Journal of Colloid and Interface Science **521**, 226 (2018).
[7] E. M. Benner and D. N. Petsev, Journal of Colloids and Interface Science **514**, 21 (2018).
[8] E. M. Benner and D. N. Petsev, in *Porous Media: Theory, Properties and Applications*, edited by D. Wolfe (Nova Science Publishers, 2016), chap. 3, pp. 87–124.
[9] E. M. Fenton, M. R. Mascarenas, G. P. López, and S. S. Sibbett, ACS Applied Materials & Interfaces **1**, 124 (2009), pMID: 20355763.
[10] S. Mendez, E. M. Fenton, G. R. Gallegos, D. N. Petsev, S. S. Sibbett, H. A. Stone, Y. Zhang, and G. P. Lopez, Langmuir **26**, 1380 (2010).
[11] C. W. N. Villarrubia, C. Lau, G. P. Ciniciato, S. O. Garcia, S. S. Sibbett, D. N. Petsev, S. Babanova, G. Gupta, and P. Atanassov, Electrochemistry Communications **45**, 44 (2014).
[12] E. Elizalde, R. Urteaga, and C. L. Berli, Lab on a Chip **15**, 2173 (2015).
[13] M. Liu, J. Wu, Y. Gan, D. A. H. Hanaor, and C. Q. Chen, Langmuir **32**, 9899 (2016).
[14] G. Hohenbichler, A. Köppl, and W. Schneider, Acta mechanica **107**, 21 (1994).
[15] C. Hall, Build. Environ. **16**, 201 (1981).
[16] P. Lehmann, S. Assouline, and D. Or, Physical Review E **77**, 056309 (2008).
[17] J. Hyväluoma, P. Raiskinmäki, A. Jäsberg, A. Koponen, M. Kataja, and J. Timonen, Phys. Rev. E **73**, 036705 (2006).
[18] J. Xiao, H. A. Stone, and D. Attinger, Langmuir **28**, 4208 (2012).
[19] R. Lucas, Kolloid Z. **23**, 15 (1918).
[20] E. W. Washburn, Phys. Rev. **17**, 273 (1921).
[21] N. Fries, K. Odic, M. Conrath, and M. Dreyer, Journal of Colloid and Interface Science **321**, 118 (2008).
[22] W. H. Green and G. A. Ampt, J. Agric. Sci. **4**, 1 (1911).
[23] D. Lockington, J.-Y. Parlange, and M. Lenkopane, Transport in porous media **68**, 29 (2007).
[24] G. M. Homsy, Annual review of fluid mechanics **19**, 271 (1987).
[25] J. O. Wilkes, *Fluid Mechanics for Chemical Engineers with Microfluidics and CFD* (Prentice Hall, New York, 2006).
[26] P. H. Moon and D. E. Spencer, *Field Theory Handbook: Including Coordinate Systems, Differential Equations and Their Solutions* (Springer–Verlag, 1988), ISBN 9783540184300.
[27] E. Shahraeeni and D. Or, Langmuir **26**, 13924 (2010).
[28] R. H. Brooks and A. T. Corey, Transactions of the ASAE **7**, 26 (1964).